Manufacturing Rev. **12**, 28 (2025)

https://doi.org/10.1051/mfreview/2025022

Manufacturing Review
Available online at:
https://mfr.edp-open.org

ORIGINAL ARTICLE OPEN ACCESS

Experimental and numerical investigations of sheet AA6082 formability and B-pillar forming under HFQ conditions

Jiaqi Li[1], Zhusheng Shi[1,2,*], Ruiqiang Zhang[1], and Jianguo Lin[1,3]

[1] Department of Mechanical Engineering, Imperial College London, London SW7 2AZ, UK
[2] Foshan Xianhu Laboratory, Foshan 528200, PR China
[3] Department of Industrial and Systems Engineering, The Hong Kong Polytechnic University, Hong Kong, PR China

Received: 31 July 2025 / Accepted: 20 October 2025

Abstract. Assessing and predicting formability of a material have significant importance for forming process design and optimisation. In this paper, formability of AA6082 under various conditions were investigated through biaxial tensile tests, and the results were used for calibrating a set of constitutive equations based on continuum damage mechanics (CDM). Forming tests that replicate industrial forming conditions were conducted to explore the effects of HFQ conditions on the formability of the AA6082 aluminium sheet. In these tests, B-pillar components of a commercial vehicle were produced under different conditions, followed by ARGUS measurements to capture the formed geometry and strain distributions. The CDM-based constitutive equations were implemented into FE model to simulate the forming processes, and the simulation results were compared with experimental data to validate the model. It was found that lower forming speed and higher temperature lead to higher formability of the material and are beneficial to the quality of the formed components. Numerical simulations successfully predicted the strain distribution and defects formed during forming and showed good agreements the experimental results from the B-pillar forming tests, indicating that the CDM-based model can be successfully applied in practical forming processes for designing and optimising the process parameters.

Keywords: Hot stamping / formability / lightweighting / constitutive modelling / aluminium alloy

1 Introduction

Lightweight materials have attracted increasing attention in the automotive industry to increase fuel efficiency and to reduce carbon emissions. To meet environmental regulations without compromise on safety standards, ultra-high-strength steels (UHSSs) and high-strength aluminium alloys have been developed specifically for critical automobile components. However, the increase of the strength of sheet metals and the decrease of the thickness of the components undermine the formability and bring challenges to produce components with complex shapes in sheet metal forming processes [1].

One of the promising solutions for high-strength aluminium alloys hot stamping is the recently developed Hot Form Quench (HFQ®) technology [2]. This technology has garnered significant attention due to its capability of producing lightweight car components with complex geometries. The HFQ process not only meets the stringent requirements of modern automotive manufacturing but also offers potential benefits in terms of material efficiency and component performance. The HFQ process was developed based on deep understanding of material behaviour at elevated temperatures [3]. The viscoplasticity, formability and damage behaviours of high-strength Al alloys are strongly influenced by the temperature and strain rate [4]. Therefore, an in-depth understanding of material properties is not only of scientific significance, but also crucial in practical production for optimising processes, saving energy, and reducing costs. In the context of metal forming, to fully exploit the capabilities of sheet metals, it is essential to precisely assess their formability, i.e. the extent to which they can be deformed without failure. Standardised methods, such as the Nakajima [5] and Marciniak tests [6], have been widely adopted in the industry for a long time and have proven reliable for assessing formability at room temperature. However, significant challenges arise when attempting to adapt these methods to evaluate forming limits under hot stamping conditions, most fatal one being the lack of capability to precisely replicate the temperature profiles during fast heating and quenching.

* e-mail: zhusheng.shi@imperial.ac.uk

Table 1. Chemical composition of AA6082 sheets (weight %).

Element	Mn	Fe	Mg	Si	Cu	Zn	Ti	Cr	Al
Min.	0.40	–	0.60	0.70	–	–	–	–	Bal.
Max.	1.00	0.50	1.20	1.30	0.10	0.20	0.10	0.25	Bal.

To address these issues, biaxial tensile tests, assisted by digital image correlation (DIC) method, have been recently developed to determine the forming limit curves (FLCs) and fracture forming limit curves (FFLCs) under elevated temperature conditions [7,8]. While these tests have shown potential for improving formability predictions, they have yet to be standardised as a widely accepted procedure for high-strength aluminium alloys, such as AA6082, and their direct application to industrial forming design remains to be validated.

Numerical simulation serves as a powerful tool for analysing these effects, but the accuracy of such simulations heavily relies on the implementation of well-calibrated material models [9]. Over the years, various models have been developed to characterise the thermomechanical properties of Al alloys under hot deformation conditions [10,11]. The experimental results of biaxial tensile tests can be directly integrated to a unified viscoplastic model based on continuum damage mechanics (CDM) [12]. While this approach has been successfully applied to ultra-high-strength steels such as 22MnB5 [12], its application to high-strength Al alloys remains limited. Moreover, its effectiveness for industrial forming processes requires further validation. Numerical simulations and finite element (FE) models must be refined to accurately capture the thermomechanical behaviour of aluminium alloys under biaxial loading conditions. Advanced material models, incorporating damage evolution and temperature-dependent properties, will be critical in improving predictive capabilities.

This research serves as a case study to validate a comprehensive biaxial formability assessment system that integrates experimental measurements with advanced numerical simulations. Biaxial formability tests under various conditions were conducted to obtain the forming limits of AA6082 aluminium alloy, and the results were utilised to calibrate a set of CDM-based constitutive equations. Forming tests replicating industrial processes were conducted on AA6082 sheets, specifically in the production of B-pillar components for commercial vehicles. ARGUS optical measurements were employed to capture the formed geometry and strain distributions. These calibrated equations were then implemented into FE models to simulate material behaviour during forming. The simulation results were compared with experimental data to evaluate the accuracy of the model and the effectiveness of the biaxial formability assessment system. The study provides valuable insights into the reliability of biaxial formability tests and their potential applications in industrial metal forming.

2 Material and methods

2.1 Characterisation of thermomechanical properties and formability

The material used in this study was aluminium alloy AA6082 sheets in T6 temper with a thickness of 1.5 mm, supplied by Smiths Metal Centres Ltd (UK). The chemical composition of the AA6082 sheets is detailed in Table 1.

Uniaxial tests and biaxial formability tests were performed to study the viscoplastic behaviours and formability of AA6082 under various conditions. The uniaxial tests were carried out with a Gleeble 3800 test machine in order to accurately replicate the realistic thermal profile during HFQ. A dogbone specimen was used in the tests, and thermocouples were welded at the midpoint of the specimen to control the temperature. The detailed procedures of the uniaxial tests can be found in [13]. Biaxial tensile tests with various strain paths were carried out to investigate the strain distribution of the cruciform specimen and the forming limits at different temperatures and strain rates for the AA6082 metal sheets. The tests were performed with the improved cruciform specimen to verify the optimisation process and obtain complete forming limit diagrams for calibrating the CDM-based constitutive equations. Figure 1 shows the cruciform specimen design, featuring notches, one-sided reduction in the centre region, and slits in the horizontal arms. This design was based on the design from Zhang et al. [14], with geometrical modifications for enhancing the validity and reliability of the biaxial formability tests. The specimens were laser-cut and then thinned at the gauge area using a computer numerical control (CNC) machine. The production of the cruciform specimens was meticulously controlled. To check the repeatability, the central thicknesses of 10 randomly chosen samples were measured using a micrometer, and all results were within a tolerance of 0.01 mm.

The biaxial tests were conducted using the Gleeble 3800 machine to reproduce the temperature history of the HFQ process, with the overall thermal profile depicted in Figure 2. To mimic the HFQ process, the specimens underwent initial heating to 535 °C at a rate of 30 °C/s, followed by 1 min soaking. A cooling rate of 60 °C/s was subsequently applied, and tensile tests were conducted at 400 °C, 440 °C and 480 °C to investigate the impact of deformation temperature. Additionally, tests were performed at different effective strain rates of 0.02, 0.1 and 0.5 /s at 440 °C to explore the influence of strain rate. For each condition, at least three different strain paths, namely equi-biaxial, plane strain and uniaxial loadings,

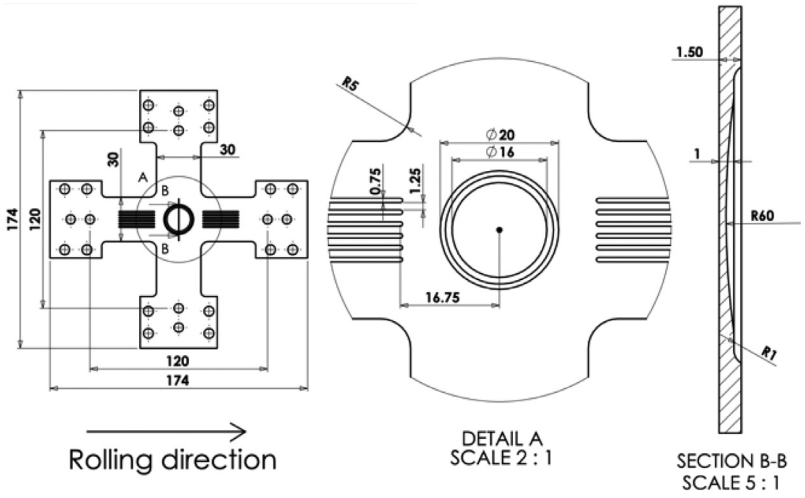

Fig. 1. Specimen geometry for biaxial formability tests.

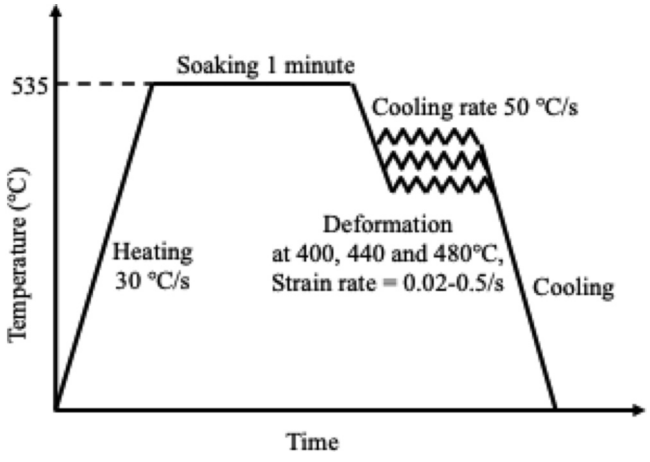

Fig. 2. The thermal profile during biaxial testing.

were applied in order to construct complete forming limit curves (FLCs). The conditions of the biaxial tests are listed in Table 2.

Despite its high-precision controlling system, the Gleeble machine is limited to provide uniaxial loadings to the specimen. Therefore, to achieve biaxial loadings with different ratios, a set of specially designed biaxial rigs was introduced. The rigs used in this study were based on the designs of Shao et al. [7] and Zhang et al. [8]. With the rigs, the input displacement from the Gleeble is converted to two orthogonal displacements Δ_1 and Δ_2, which are transferred to the horizontal and vertical arms of the cruciform specimen.

Using the biaxial rigs, different loading paths can be achieved by applying different displacement ratios $\beta_d = \Delta_2/\Delta_1$. In ideal biaxial tests, one objective is to find a function $\Delta_1(t)$ that can produce a constant effective strain rate. Under von Mises yield criterion, the effective strain rate $\dot{\varepsilon}_e$ is defined as:

$$\dot{\varepsilon}_e = \frac{\mathrm{d}\varepsilon_e}{\mathrm{d}t} = \sqrt{\frac{2}{3}\dot{\varepsilon}'_{ij}\dot{\varepsilon}'_{ij}} = \sqrt{\frac{2}{9}\left[(\dot{\varepsilon}_1-\dot{\varepsilon}_2)^2+(\dot{\varepsilon}_2-\dot{\varepsilon}_3)^2+(\dot{\varepsilon}_3-\dot{\varepsilon}_1)^2\right]} \quad (1)$$

where $\dot{\varepsilon}'_{ij}$ represents the deviatoric strain rate, and $\dot{\varepsilon}_1$, $\dot{\varepsilon}_2$, $\dot{\varepsilon}_3$ the principal strain rates. The plastic strains in the tests are typically large, so the elastic strain is neglected. Constant volume is assumed, thus $\mathrm{d}\varepsilon_1 + \mathrm{d}\varepsilon_2 + \mathrm{d}\varepsilon_3 = 0$. If the strain path is linear, $\beta_e = \varepsilon_2/\varepsilon_1 = \mathrm{d}\varepsilon_2/\mathrm{d}\varepsilon_1$, and equation (1) can be rewritten as:

$$\dot{\varepsilon}_e = \sqrt{\frac{2}{9}\left[(1-\beta_e)^2+(1+2\beta_e)^2+(2+\beta_e)^2\right]}\dot{\varepsilon}_1. \quad (2)$$

Therefore, for a given strain ratio β_e, the effective strain rate $\dot{\varepsilon}_e$ can be converted to the strain rate of horizontal direction $\dot{\varepsilon}_1$. The input displacement in the horizontal direction Δ_1 can thus be calculated by the relationship $\Delta_1 = L_{c1}\exp(\dot{\varepsilon}_1 t - 1)$, like in conventional uniaxial tensile tests, where L_{c1} is the characteristic gauge length. However, complications arise due to the complex interaction of temperature gradients, specimen geometry, and strain rate heterogeneity, leading to significant strain localisation from the onset of deformation. As a result, the strain ratio $\beta_e = \varepsilon_2/\varepsilon_1$ does not generally coincide with the ratio of input displacements β_d, posing difficulties in controlling the effective strain rate in the biaxial tests. In this study, L_{c1} was empirically chosen as 4 mm, and the relationships of β_d and β_e obtained from preliminary tests are shown in Table 3.

In the biaxial tests, the specimens were resistance heated to reach a target temperature, achieved by the Gleeble controller's feedback mechanism, monitoring the temperature values from thermocouples welded onto the specimen. In biaxial tests, the cruciform specimen cannot be directly connected to the jaws; rather, the arms of the specimen and the Gleeble jaws were linked via additional cables between them. In this study, cables with braided fibreglass and mica sleeving were chosen for their excellent high-temperature resistance. The upper arm of the specimen was connected to the positive electrode and the lower arm was connected to the negative electrode. Prior to biaxial tensile tests, temperatures at various locations within the reduction area were investigated using thermocouples to evaluate the temperature uniformity.

Table 2. Conditions of biaxial tests, E for equi-biaxial loading, P for plane strain loading and U for uniaxial loading.

Strain rate \ Temperature	400 °C	440 °C	480 °C
0.02 /s		E, P, U	
0.1 /s	E, P, U	E, P, U	E, P, U
0.5 /s		E, P, U	

Table 3. Relationships of strain ratio β_e and displacement ratio β_d.

Target strain state	β_e	β_d
Equi-biaxial	1	1
Plane strain	0	0.18
Uniaxial	−0.5	−0.18

It was found that under all tested conditions, the maximum temperature difference was lower than 5 °C in the 6 mm diameter central area, within which fracture initiates in all valid tests.

The FLCs were constructed by connecting data points of limit strains, which can be determined using various methods [15–17]. In this study, the spatio-temporal method proposed by Zhang et al. [18] was employed to determine the necking and fracture forming limits from biaxial formability tests. In this method, after the test, two distinct zones are defined around the fracture initiation site: a smaller base zone (BZ) and a larger reference zone (RZ), as illustrated in Figure 3a. During the initial stage of uniform deformation, the thickness reduction, ε_3, is uniform across both zones. As deformation progresses, strain begins to concentrate within the BZ, resulting in divergence between $\overline{\varepsilon}_3^{\mathrm{BZ}}$ and $\overline{\varepsilon}_3^{\mathrm{RZ}}$, respectively the average thickness reduction in the BZ and the RZ. The onset of necking is designated as the point at which the divergence between $\overline{\varepsilon}_3^{\mathrm{RZ}}$ and $\overline{\varepsilon}_3^{\mathrm{BZ}}$ reaches a certain extent, which is reflected by the significant change in slope on the $\overline{\varepsilon}_3^{\mathrm{RZ}}$-$\overline{\varepsilon}_3^{\mathrm{BZ}}$ curve. In practice, two straight lines are linearly fitted from the initial and final portions of the curve, and their intersection is used to define the experimental onset of necking, as illustrated in Figure 3b. In this study, data points before $t/t_{\mathrm{F}} = 0.5$ were selected for fitting the first straight line and points after $t/t_{\mathrm{F}} = 0.9$ were selected for fitting the second straight line. Once the thickness reduction at necking is determined, the corresponding major and minor strains at the same time step can subsequently be found and designated as the forming limits of the sheet metal.

In this study, the BZ and RZ were set rectangles with the same height but different widths. Furthermore, the orientations of these zones were set perpendicular to the direction of fracture, where maximum in-plane major strain occurs, ensuring an accurate representation of the strain distribution and improving the reliability of the results. According to the principle of the spatio-temporal method, the size of BZ should be comparable to the size of the necking band. However, defining the necking band becomes more challenging in high-temperature tests with heterogenous temperature distribution, because in these tests no uniform deformation stage exists even in the initial stages of the process. To address this issue, it is essential to limit the size of the BZ to an area where the temperature gradient is minimal, ensuring that temperature-induced variations do not significantly impact the accuracy of the evaluation. Similarly, the size of the RZ must also be small enough to maintain a relatively uniform temperature field; meanwhile, it should also be large enough to be distinguished from the BZ. In this study, based on the temperature distribution across the cruciform specimen, the width of the RZ (W_{RZ}) was set to 3 mm, ensuring that the temperature gradient within this area is less than 5 °C when the central temperature is 500 °C. Correspondingly, W_{BZ} was set to 1.5 mm, half of the RZ width, while the height W_{L} of both the BZ and RZ was set to 2 mm. This configuration allows for a reliable and accurate evaluation of the necking and fracture forming limits under the high-temperature testing conditions.

The strain distribution data for the biaxial tests were captured using DIC techniques, and the resulting images were processed in the GOM Correlate software. In the software, local strain values are the average strain values measured by a virtual extensometer with a very short effective virtual strain gauge length (VSGL). In this study, the VSGL was set to the size of a pixel, approximately 0.76 mm. By matching with the records generated by the Gleeble machine, the beginning of deformation was identified and the captured image series were labelled with time stamps. The time stamp of the first image frame with a visible crack was designated as the onset of fracture, and the corresponding local strain at the fracture was taken as the fracture strain. Because of the nature of serial image capturing, the exact time of fracture initiation may fall in between two frames, leading to relatively larger variation of fracture strain than the necking strain. To obtain the average thickness reduction within the BZ and RZ, the following steps were taken:

- Identify the fracture initiation point in the image where the specimen begins to crack. This point serves as the centre point for both the BZ and RZ.
- Compute the major strain direction at the fracture initiation point. This direction will be used as the orientation of the long side of the RZ.
- Define BZ and RZ on the initial undeformed image. Using the fracture initiation point as the centre, the BZ and RZ are drawn with their long sides aligned with the major strain direction, with the predefined sizes and shapes.
- Compute the average thickness reduction within the BZ and RZ. In the 2D DIC analysis, the thickness reduction is derived from the in-plane major and minor strains

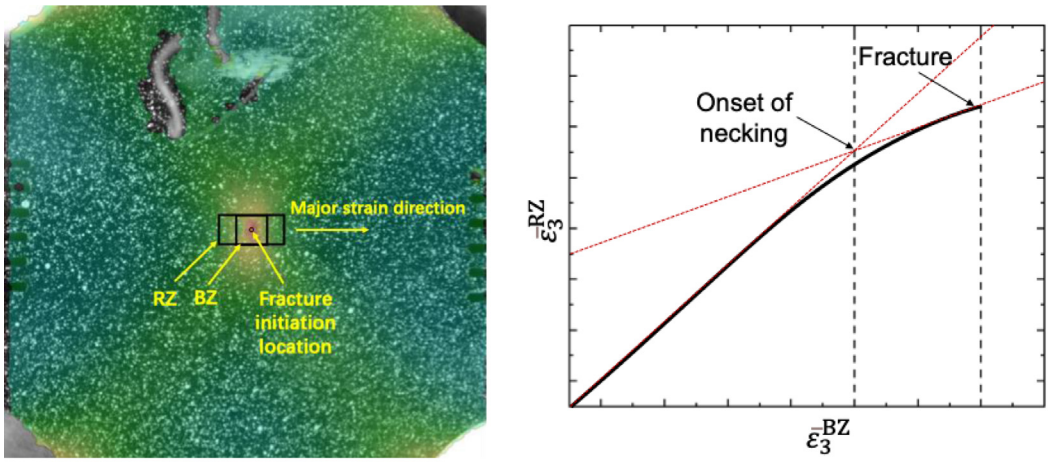

(a) Definitions of BZ and RZ (b) Determination of onset of necking

Fig. 3. Schematics of the spatio-temporal method to determine the onset of necking. (a) shows the definitions of base zone (BZ) and reference zone (RZ), and (b) demonstrates the intersection point of average thickness reductions of RZ and BZ as the onset of necking.

under the constant volume assumption, and the average thickness reductions within both BZ and RZ are calculated.

Following these procedures, the BZ and RZ in biaxial tests were clearly defined, and the average thickness reductions $\bar{\varepsilon}_3^{RZ}$ and $\bar{\varepsilon}_3^{BZ}$ were extracted.

2.2 B-pillar forming tests

Practical B-pillar forming tests were performed to verify the forming limits and the developed constitutive model for AA6082. The experimental setup, shown in Figure 4a, comprised an ESH 25T press machine equipped with controlling system, a specially designed tool for manufacturing a B-pillar component, and a furnace for heating the sheet metal. The forming tool, mainly consisted of a die, a punch and a blank holder (Fig. 4b), was installed in the press machine. The geometries of the die and the punch, as well as the dimensions of the formed part, are shown in Figure 4c. The materials used in the experiment were AA6082 sheets with a dimension of 310 mm ×200 mm × 2 mm.

The forming tests were carried out at various temperatures and forming speeds, as listed in Table 4. It is noteworthy that it is difficult to control the strain rate in the forming tests, and instead forming speeds were selected as the controlling parameter. All the tools were kept at room temperature before the forming tests. Temperature measurements were conducted with *K*-type thermocouples, which were fixed through pre-drilled holes on the side of the sheets. The forming speed was controlled by the press machine. Prior to testing, Omega 35 high-temperature lubricant (Sovereign Lubricants, UK) was carefully applied to the die and the punch. The overall thermal profile during the tests is the same to what is illustrated in Figure 2. The sheet metal was first heated in a furnace to the solution heat treatment (SHT) temperature, and was subsequently soaked for 1 min. The sheet was then taken out and positioned between the die and the blank holder, where it cooled to the deformation temperature. Once the sheet reached the desired temperature, it was promptly formed with a defined speed. The formed part was in-die quenched and removed when it cooled down to room temperature. The controlling software of the press machine automatically captured the force and stroke data throughout deformation, while temperature readings from the thermocouples were recorded using PicoLog software via a data logger.

To assess deformations and strain distributions of the formed components, GOM ARGUS system was utilised. Before deformation, metal sheets were marked with a dot pattern prepared by electro-chemical etching with an etching grid to produce reference features. The dots had a diameter of 0.75 mm and the grid spacing was 1.5 mm. After the forming tests, photographs of the formed components were taken using a Canon EOS 60D digital camera with a focal length of 135 mm. During the capturing process, the part was positioned on a turntable, surrounded by coded markers used for the spatial coordinate calibration. The camera, mounted on a tripod, captured views from different angles and heights by rotating the turntable and adjusting the height of the tripod. In accordance with the recommendations from the ARGUS manual, photos from at least 8 different directions at 3 height levels were taken for each formed part, and at least 4 coded points should be clearly visible in each photo. The relative position of the part and the markers were kept unchanged until the analysis was completed, allowing supplementary views to be taken after an initial analysis.

The photos were imported into the GOM ARGUS software for analysis. Based on predefined parameters of the lens and the coded markers, the software automatically identified the coded points and established the spatial coordinates according to their relative positions in different images. While the software could also automatically recognise feature points on the components, manual matching of many points was necessary due to damage to the dot pattern or poor image quality in certain areas because of deformation and sheet-tool contact. The measured 3D surface geometries and strain distributions were subsequently compared with simulated results for validating the numerical model.

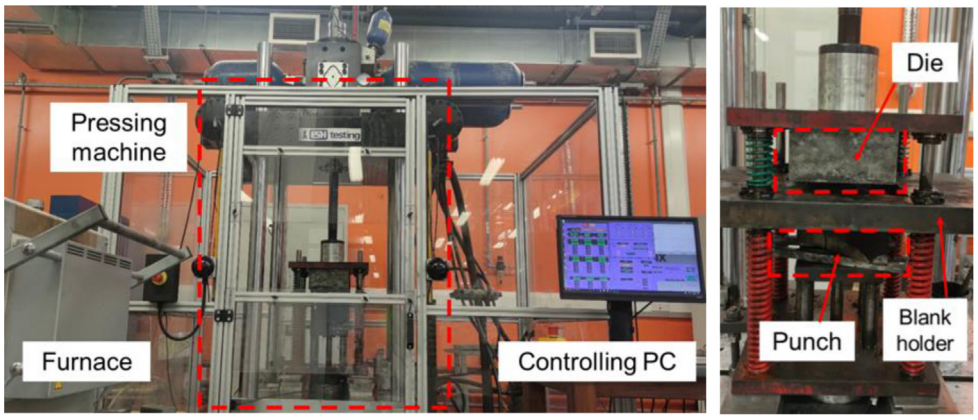

(a) Overall setup (b) Layout of tools

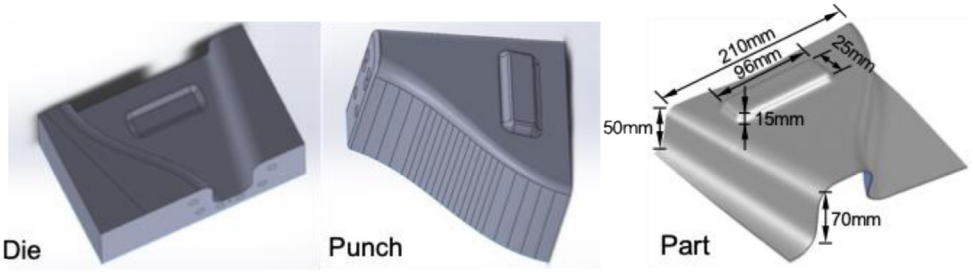

(c) Geometries of tools and the part

Fig. 4. The experimental setup of the B-pillar forming test system.

Table 4. Conditions of B-pillar forming tests.

Forming speed \ Temperature	400 °C	440 °C	480 °C
50 mm/s		√	
250 mm/s	√	√	√
350 mm/s		√	

2.3 FE simulations

FE simulations were carried out using the commercial software Abaqus/Explicit, replicating the forming process under various forming temperatures and speeds. Figure 5 shows the layout of the FE model used for the forming simulation. In this model, the punch, the die and the blank holder were treated as rigid bodies. Both the die and the blank holder were set completely fixed, meaning they had no displacement or rotation throughout the process, while the punch was allowed to move along the z-direction. When the simulation step started, the punch moved towards the sheet metal with a predefined forming speed, until the gap between the punch and the die matched the thickness of the sheet (2 mm). A friction coefficient of 0.3 was applied to the contact surfaces between the blank and the tools. The constitutive and damage models were implemented into the FE simulation using a VUMAT subroutine to describe the material behaviour and damage at various

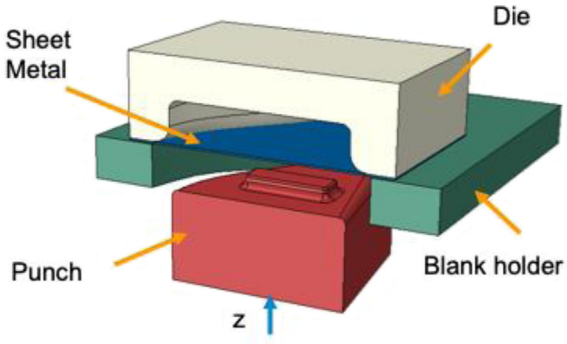

Fig. 5. Schematic FE model for forming the B-pillar part.

temperatures and strain rates. In the simulations, 8-node linear 3D solid elements with reduced integration (C3D8R) and hourglass control were applied. The mesh size of the sheet metal was set to 1 mm, which was finer than the resolution of ARGUS measurement and the accuracy had been verified with trial simulations.

3 Results and discussion

3.1 FLCs and FFLCs for AA6082

Proper fracture initiation near the centre of the cruciform specimen is crucial for ensuring the validity of the test, as only the test conditions within the central region of the

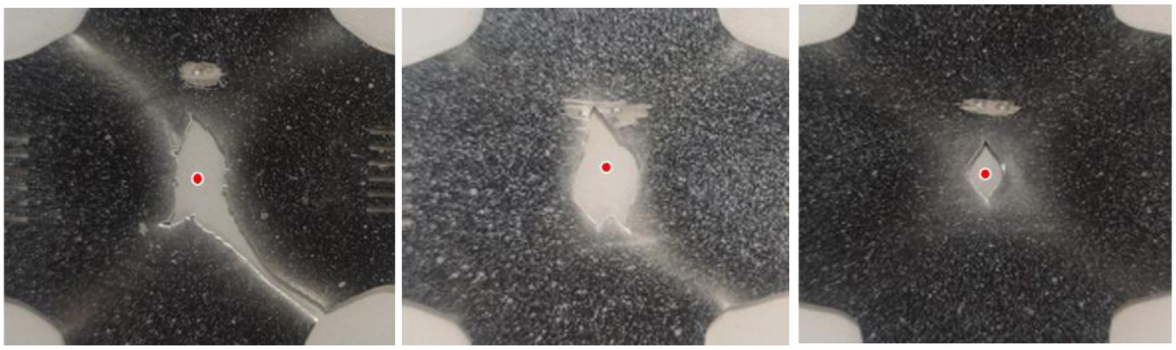

(a) Equi-biaxial (b) Plane strain (c) Uniaxial

Fig. 6. Fracture initiation locations (marked as red dots) at different loading conditions in the biaxial tests.

specimen can be precisely controlled. In the biaxial tests conducted in this study, fracture consistently occurred around the centre of the specimen under all loading paths, as illustrated in Figure 6, thereby confirming the validity of the test results. Thinning was primarily observed within the gauge area, and during the tests, the fracture gradually propagated towards the notches of the cruciform specimen (the four corners in the figure). Under equi-biaxial loading, deformation at the notches was also noticeable; however, it was not significant enough to induce premature fracture in those regions.

Fig. 7a presents the distribution of major strain across the gauge area of the specimen, under equi-biaxial loading, with a central temperature of 440 °C and a nominal strain rate of 0.1 /s. The images were captured at a near-fracture stage, specifically at $t/t_F = 0.99$, where t represents the time elapsed since the start of the test, and t_F denotes the time at which fracture initiates. The results indicate that, in addition to the centre where the fracture initiates, strain localisation was also observed near the four notches. Nevertheless, the strain levels at the notches were lower than those at the centre, ensuring that fracture occurred within the gauge area. Along the lines connecting the centre and the notches, intermediate levels of major strain formed an X-shaped pattern, outside of which the major strain levels were much lower. The distribution of the major strain directions, shown in Figure 7b, reveals that the major strain field exhibits concentric circles around the centre of fracture initiation. The pattern of major strain directions displayed both bilateral symmetry and near-centrosymmetry, indicating a typical equi-biaxial strain state. These observations confirm the effectiveness of the specimen design and biaxial testing method.

Figure 7c shows the distribution of major strain across the gauge area in the specimen under a plane strain loading path, with the same central temperature and nominal strain rate, also at $t/t_F = 0.99$. A similar X-shaped pattern was observed; however, different from what was found in equi-biaxial loading (Figs. 7a and Figs. 7b), it can be seen that under plane strain state, strain localisation near the notches was absent, while the centre became the sole region exhibiting high strain level. Figure 7d illustrates the distribution of the major strain directions under plane strain loading. Unlike the equi-biaxial case shown in Figure 7b, the major strain directions under plane strain loading tended to align with the horizontal axis, corresponding to the direction of the applied displacement.

Similar trends were found in the biaxial tests conducted under a uniaxial loading path, as shown in Figure 7e and Figs. 7f. Both the strain distribution and the directions were similar to those observed under plane strain conditions, although the horizontal deformation under uniaxial loading was more pronounced.

Using the spatio-temporal method, the limit strains at the onset of necking and fracture were determined from biaxial formability tests. The characterised limit strains are displayed in Figure 8, where hollow markers represent the limit strains at the onset of necking, and solid markers indicate fracture strains. The data indicates a general trend that lower strain rates and higher temperatures lead to higher necking and fracture strains. This observation aligns with general trends in material formability, where higher temperatures and lower strain rates typically reduce the extent of strain localisation, thereby increasing the material's formability. It is also observed that the effect of temperature and strain rate on the forming limit of AA6082 is limited, within about 0.1 of major strain for the tested conditions at specific loading paths. It is noteworthy that shapes of the FLCs and FFLCs are not the same. The FLCs had more pronounced upward curvature tail at the equi-biaxial side, while the FFLCs tended to be closer to straight lines. This suggests that under equi-biaxial loading state, the onset of fracture is closer to the onset of necking, which is consistent with the experimental results of FLC and FFLC for AA5086 sheets from Song et al. [19]. It should be noted that due to the relatively larger uncertainty of the exact time and locations of fracture initiation, the characterised fracture strain levels were not as stable as the necking strains that formed the FLCs. As a result, discrepancies were found more pronounced in FFLCs, which are therefore taken as complimentary criteria in the formability assessment.

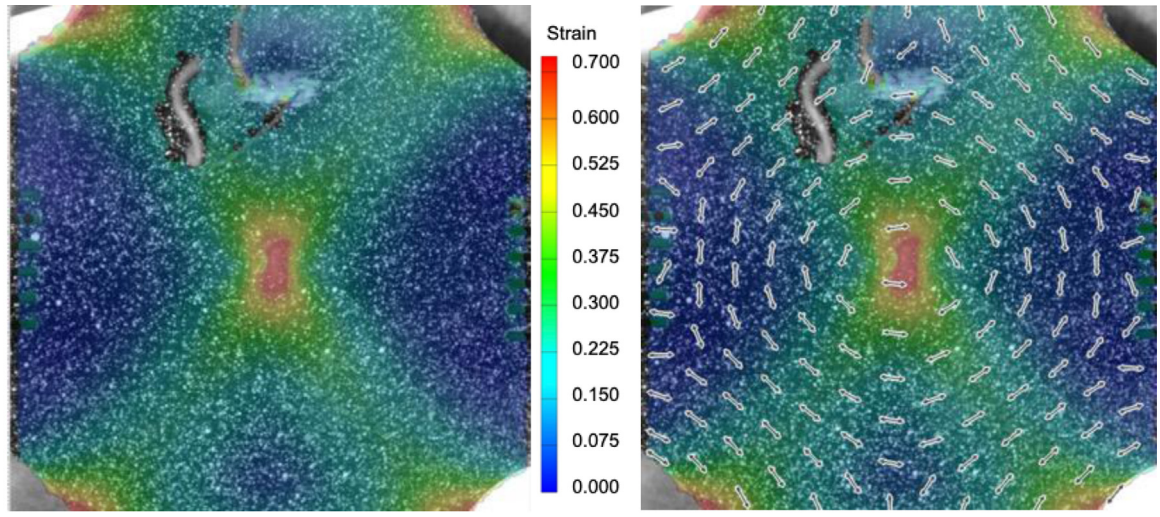

(a) Major strain distribution, equi-biaxial (b) Major strain direction, equi-biaxial

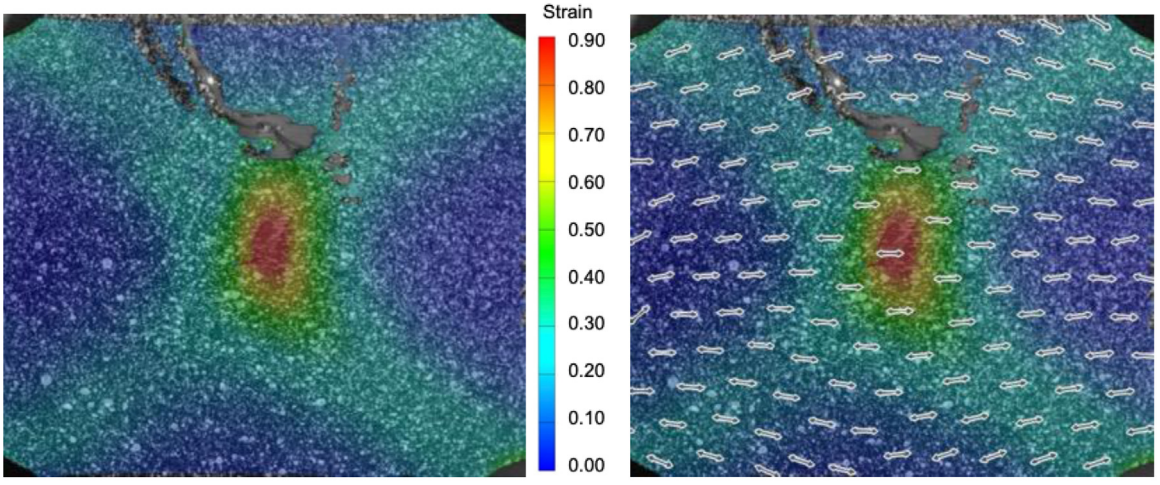

(c) Major strain distribution, plane strain (d) Major strain direction, plane strain

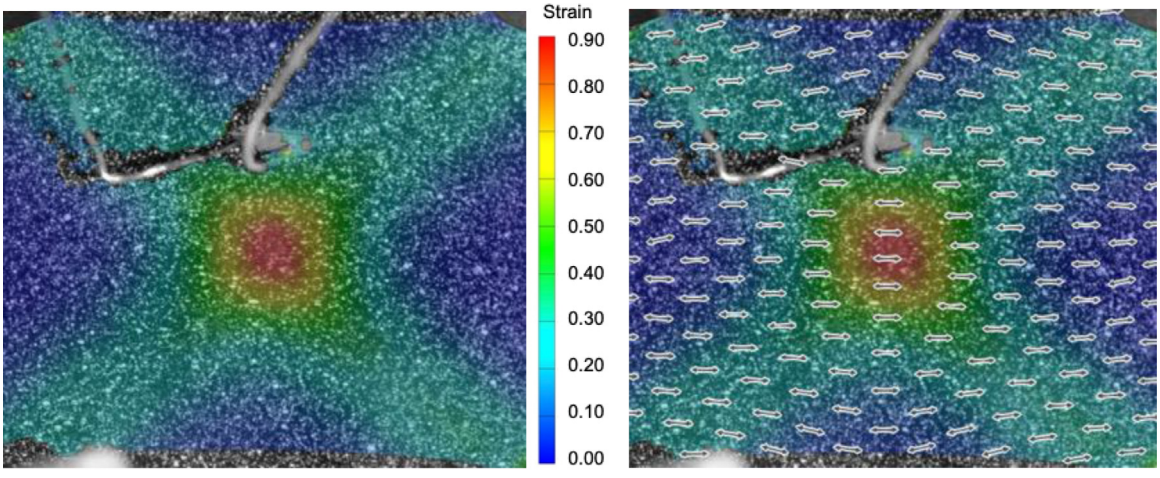

(e) Major strain distribution, uniaxial (f) Major strain direction, uniaxial

Fig. 7. Distribution of major strain and its direction for different loading conditions when $t/t_F = 0.99$, after forming at 440 °C and 0.1 /s.

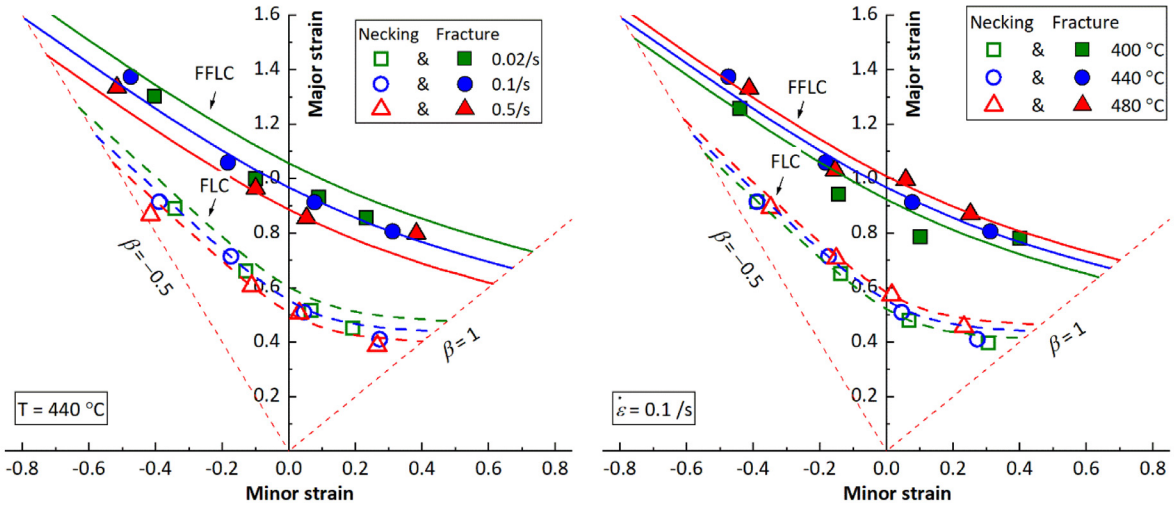

(a) FLCs and FFLCs under different strain rates (b) FLCs and FFLCs under different temperatures

Fig. 8. FLCs and FFLCs constructed using experimental data. The symbols are experimental data and the lines are computed FLCs and FFLCs using the calibrated CDM-based model.

3.2 CDM-based constitutive model

To simulate the damage in the forming simulations, the necking and fracture behaviours of the sheet metal should be defined in the constitutive equations. To achieve this, a set of constitutive equations, based on continuum damage mechanics (CDM), was applied. These equations, proposed by Zhang et al. [12], were derived based on the unified viscoplastic constitutive equations from Lin and Dean's work [20], with major modifications being the introduction of two damage state variables ω_1 and ω_2, representing the extent of necking and fracture, respectively. In hot stamping, the limit strain at fracture is used as a complementary tool for assessing the formability of the material. The two state variables are correlated with each other, take similar forms as pioneering works such as [21] and [22]. A correcting term $1/[(1-\omega_1)(1-\omega_2)^{\eta_1}]$ was added to the expression of the effective plastic strain rate $\dot{\varepsilon}_e^p$. The CDM-based unified viscoplastic constitutive equations are constructed as below:

$$\begin{cases} \dot{\varepsilon}_e^p = \left(\dfrac{\sigma_e - R - k}{K}\right)^{n_1} \dfrac{1}{(1-\omega_1)(1-\omega_2)^{\eta_1}} \\ \dot{R} = 0.5B\bar{\rho}^{-0.5}\dot{\bar{\rho}} \\ \dot{\bar{\rho}} = A(1-\bar{\rho})\left|\dot{\varepsilon}_e^p\right| - C\bar{\rho}^{n_2} \\ \dot{\varepsilon}_{ij}^p = \dfrac{3}{2}\dfrac{S_{ij}}{\sigma_e}\dot{\varepsilon}_e^p \\ \sigma_{ij} = D_{ijkl}\left(\varepsilon_{ij} - \varepsilon_{ij}^p\right) \\ \dot{\omega}_1 = \left[\dfrac{D_1}{(\mu_1 - 0.5\mu_2)^{\phi_1}}\right]\left(\dfrac{\mu_1\varepsilon_1 + \mu_2\varepsilon_2}{\gamma + \varepsilon_e^p}\right)^{\phi_1} \dfrac{1-\omega_1}{(1-\omega_2)^{\eta_1}}\left(\dot{\varepsilon}_e^p\right)^{\eta_2} \\ \dot{\omega}_2 = \left[\dfrac{D_2}{(\mu_1 - 0.5\mu_2)^{\phi_2}}\right]\left(\dfrac{\mu_1\varepsilon_1 + \mu_2\varepsilon_2}{\gamma + \varepsilon_e^p}\right)^{\phi_2} \dfrac{1}{(1-\omega_1)(1-\omega_2)^{\eta_1}}\left(\dot{\varepsilon}_e^p\right)^{\eta_2} \end{cases} \quad (3)$$

where σ_e is the effective flow stress, ε_e^p the effective plastic strain, ε_1 and ε_2 the major and minor in-plane strains, ε_{ij}^p and σ_{ij} the components of the plastic strain and stress tensors, S_{ij} the components of the deviatoric stress tensor, R the stress due to isotropic hardening, k the initial yield stress, $\overline{\rho}$ the normalised dislocation density, D_{ijkl} the components of the elasticity tensor, and k, K, n_1, n_2, A, B, C, D_1, D_2, μ_1, μ_2, ϕ_1, ϕ_2, η_1, η_2 and γ are material constants. The first four equations are based on studies of Lin et al. [20,23], which embedded the effect of dislocation density into a power-law viscoplastic model. The fifth equation is the generalised Hooke's law, and the last two equations describe the evolution of the two damage state variables ω_1 and ω_2. In this study, critical values for ω_1 and ω_2 are set to 0.7, representing the threshold values for the onset of necking and fracture, respectively. The material constants k, K, n_1, B, D_1, μ_1, ϕ_1, η_2, D_2, ϕ_2 are temperature-dependent and take the form of

$$x = x_0 \exp\left(\frac{Q_x}{R_g T}\right) \quad (4)$$

where x represents each material constant listed above, R_g the gas constant ($8.314\ \mathrm{J\cdot K^{-1}\cdot mol^{-1}}$), and Q_x is an energy term corresponding for the constant x. C is also a temperature-dependent material constant and takes the form

$$C = C_0 \exp\left(\frac{-Q_c}{R_g T}\right). \quad (5)$$

Based on whether damage is involved, the constants can be grouped into two sets. Therefore, a 2-stage fitting procedure was applied. In the first stage, constants related

Table 5. Calibrated material constants in the viscoplastic constitutive equations.

Constant	k_0	Q_k	K_0	Q_K	n_{1_0}	Q_{n_1}	B_0	Q_{B}	A	C_0	Q_{C}	n_2
Unit	(MPa)	(J/mol)	(MPa)	(J/mol)	(−)	(J/mol)	(MPa)	(J/mol)	(−)	(s^{-1})	(J/mol)	(−)
Value	0.36	2.04×10^4	0.50	2.50×10^4	5.12	100	1.00	1.97×10^4	0.10	5.00	2400	1.16

Table 6. Calibrated damage-related constants.

Constant	D_{1_0}	Q_{D_1}	μ_{1_0}	Q_{μ_1}	μ_2	ϕ_{1_0}	Q_{ϕ_1}	γ
Unit	(−)	(J/mol)	(−)	(J/mol)	(−)	(−)	(J/mol)	(−)
Value	0.27	7388	0.31	210.8	0.15	4.08	382	3.5×10^{-3}
Constant	η_1	η_{2_0}	Q_{η_2}	D_{2_0}	Q_{D_2}	ϕ_{2_0}	Q_{ϕ_2}	
Unit	(−)	(−)	(J/mol)	(−)	(J/mol)	(−)	(J/mol)	
Value	5	0.99	382	2.25×10^{-2}	5273	1.36	382	

to the viscoplastic constitutive relationship of the material were calibrated using the experimental data obtained in the uniaxial tests. To avoid the damage effects, the last two equations in equation (3) were removed and the correcting term $1/\left[(1-\omega_1)(1-\omega_2)\right]^{\eta_1}$ was omitted. The MATLAB function "lsqnonlin", included in the Optimization Toolbox, was used to conduct the nonlinear data fitting. A fitting method involving varying strain rate was applied to improve the reliability of the calibration. The details of fitting method and the uniaxial test results can be found in [13]. The calibrated values for material constants in this stage are listed in Table 5.

The damage-related parameters were determined by fitting the damage-related equations with the experimental data points for the limit strains obtained from biaxial formability tests (Fig. 8). Due to the limited number of experimental data points available for the limit strains, the damage-related constitutive equations at 440 °C were fitted manually by iteratively adjusting the parameters to achieve a satisfactory match with the experimental data. Once a good fit was achieved for the data at 440 °C, temperature-dependent parameters were determined by fitting the experimental data at different temperatures. These constants are listed in Table 6. Using these calibrated parameters, the FLCs and FFLCs were computed and plotted with solid lines in Figure 8. A comparison of these computed curves with the experimental data points reveals a good agreement, validating the fitting process. However, it should be pointed out that due to the uncertainties in the stages of fracture strain determination, more obvious discrepancies between experimental and fitted results were found at the FFLCs, especially those obtained at the 440 °C, 0.5/s and 400 °C, 0.1/s. The trends observed in the fitted curves indicate that higher temperatures and lower strain rates lead to higher limit strains at both the onset of necking and fracture, consistent with expected material behaviour during forming processes.

3.3 Characterisation and model prediction of formed B-pillar

Figure 9a shows the photos of the formed B-pillar components under different forming temperatures and speeds. The forming conditions did not much influence on the overall shapes of the formed components. While no macroscopic fracture was observed in the samples, necking was found to have occurred at the raised structure (marked by yellow rectangle in Fig. 9) of the components. The details of necking in the raised structure are demonstrated in Figure 9b. To define the necking locations, two shorter edges at the upper part of the raised feature are labelled as Edge A and Edge B, with four vertices designated with a_1, a_2, b_1 and b_2, as shown in Figure 9b. It was observed that Edge A, located on the side nearer the curved shape, was more prone to necking, whereas no significant necking was found along Edge B on the opposite side with straight boundary.

The results for necking under various conditions are illustrated in Figure 10, which reveal that the location and severity of necking are influenced by both temperature and forming speed. In some cases, such as the part formed at 400 °C and 440 °C under a forming speed of 250 mm/s, obvious necking can be spotted, while in other cases the necking appeared less significant or negligible. The data demonstrates a consistent trend: necking predominantly occurred along Edge A, particularly at Vertex a_1, which proved to be the most susceptible under conditions of lower temperatures and/or higher forming speeds. For example, in the part formed at 400 °C with a speed of 250 mm/s, necking not only concentrated at Vertex a_1 but extended toward Vertex a_2, indicating a more severe material thinning along Edge A. In contrast, the vertices along Edge B (b_1 and b_2) consistently showed no significant necking across all forming conditions investigated in this study. Furthermore, forming at higher temperatures and lower speed, such as 440 °C at 50 mm/s or 480 °C at 250 mm/s, appeared to improve material ductility and alleviate stress

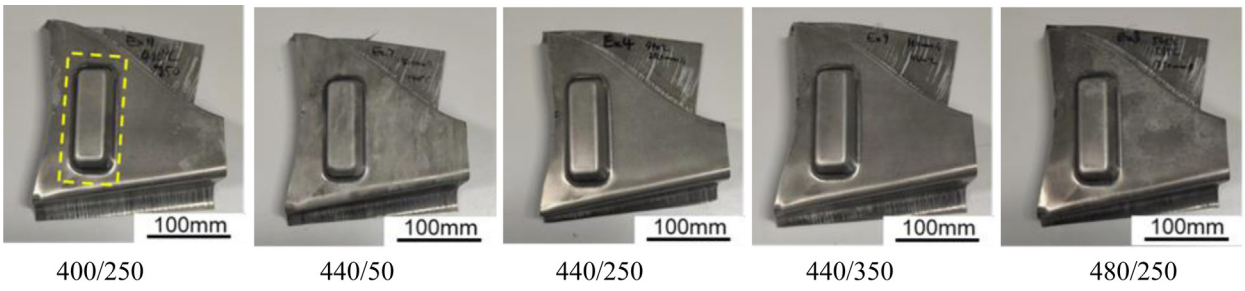

(a) Formed B-pillar components under different forming conditions

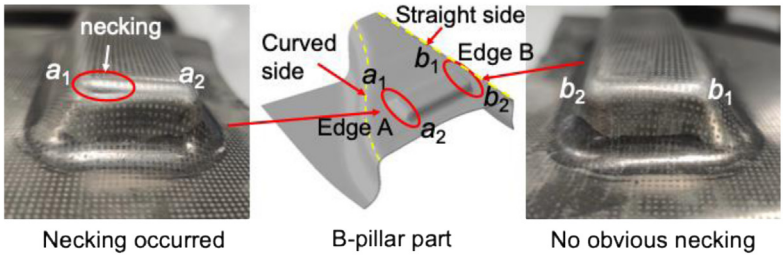

(b) Necking locations in the formed components.

Fig. 9. Photos of B-pillar components formed under different forming conditions. The numbers show the forming temperature in °C /forming speed in mm/s).

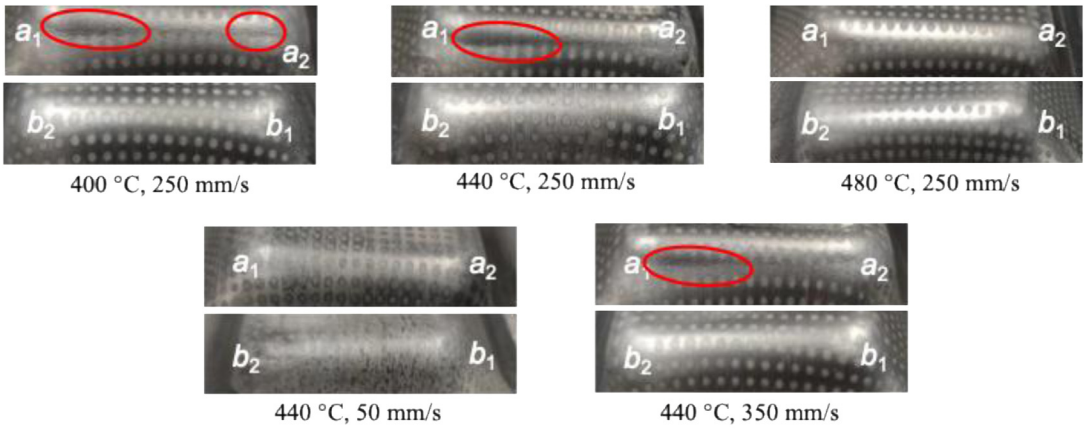

Fig. 10. The morphology of necking (marked with red circles) under different forming conditions.

concentrations, consistent with forming limit results, leading to higher part quality with minimal or negligible necking. This suggests that optimising the forming temperature and speed can effectively control necking and improve the uniformity of strain distribution in the final component.

The locations and extent of necking are attributed to the part's asymmetric geometry. Because the side with the curved shape has a longer and more complex profile, it requires greater material flow to achieve the desired contour. This increased demand of material flow leads to higher stretching and strain concentration along Edge A, where material is constrained by the surrounding features, amplifying the tendency for necking. The necking locations under different conditions are summarised in Table 7.

With the aid of the ARGUS optical measurement technique, the strain distributions of the formed components were evaluated. Figures 11a–Fig. 11d show the computed fields of major strain, minor strain, von Mises strain, and thickness reduction for the forming tests at forming temperatures of 400, 440 and 480 °C, with a forming speed of 250 mm/s.

As illustrated in Figure 11a, the locations near the Vertex a_1 on Edge A exhibited highest major strains across all three conditions, with the second highest major strain often occurred near Vertex a_2. Additionally, Vertex b_1 and b_2 on Edge B were also identified as primary sites of major strain concentration. Similar patterns were observed in the distributions of von Mises strain and thickness reduction. These results closely aligned with the necking locations

Table 7. Necking locations.

Test #	Forming Temperature (°C) / Forming Speed (mm/s)	Necking location
1	400 / 250	a_1 a_2
2	400 / 250	a_1 a_2
3	440 / 50	a_1 (Slight)
4	440 / 50	None
5	440 / 250	a_1
6	440 / 250	a_1
7	440 / 350	a_1
8	440 / 350	a_1
9	480 / 250	a_1 (Slight)
10	480 / 250	a_1
11	480 / 250	a_1

reported in Table 7. In contrast, the maximum minor strains, shown in Figure 11b were predominantly located near the corners but were concentrated on the top surface of the raised structure near a_1, where necking was more prevalent. From the figures, it is seen that the strain distributions under different forming temperatures were very similar, despite that the tests with lower temperatures exhibited marginally higher strain levels at localised deformation spots. However, due to the limitations of the measurement method, areas with large local deformation are prone to larger measurement errors. Consequently, the strain results, particularly in localised deformation zones, were interpreted qualitatively rather than quantitatively.

Figure 12 shows the simulated results, including the location and the level of maximum strain, together with the experimental results. A good agreement was found between the simulated and experimental major strain distributions. In both experimental and simulated strain distributions, strain concentration was found at the corners of the raised feature, exhibiting a maximum major strain level of 0.8 to 1.0. In addition to the vertices, the four edges at the upper part of the raised feature also exhibited considerable strain concentration, with strain levels of approximately 0.4 to 0.6. Similar to what were shown in the ARGUS measured results, the strain distributions were very similar across different conditions, although slight differences were observed around the strain localisation spots.

The force and stroke during the forming procedure at 440 °C, 250 mm/s are shown in Figure 13. The forces were given in negative values to represent compressive forces. From the curve of recorded force, it is observed that the forming force suddenly increased when the die was closing and reached its maximum value when the die was closed, and then gradually decreased to a more stable value during holding due to the stress relaxation. The dashed line demonstrated the simulated force evolution from FE results. Very good agreement was observed between the tested and simulated results, especially during the holding stage.

Table 8 compares the tested and simulated holding forces under different forming temperatures. In both the experimental and simulated data, it is evident that lower temperatures lead to increased forces. This is due to the increased resistance to deformation at lower temperature. This trend also correlates with the observed occurrence of necking. Lower forming temperatures make the material more prone to necking due to reduced ductility. The good agreement between the simulated and tested forces showcased the reliability of the constitutive equations and the FE model.

4 Conclusions

This paper investigates the formability (FLCs and FFLCs) of AA6082 through biaxial tensile tests and forming of B-pillar components. Based on the results, a set of CDM-based constitutive equations were calibrated to model the material behaviour under various HFQ conditions. A good agreement was achieved between experimental and FE simulation results on the HFQ processing of AA6082 B-pillar components. Key findings and contributions of this study are summarised as follows:

- Complete FLCs and FFLCs for AA6082 under various temperatures and forming speeds were successfully constructed. The necking and fracture strains increased with increasing temperature and decreasing strain rate.
- A set of CDM-based constitutive equations were calibrated with the experimental results to model the behaviour of damage parameters. The model can be employed to predict necking and fracture strains under various HFQ conditions.
- With the determined constitutive equations, FE simulations accurately predicted strain distributions, defect locations and forming force in a close agreement with experimental data, demonstrating their effectiveness in real-world forming processes.
- Necking was found most likely to occur on the edge of the raised structure near the curved side of the B-pillar due to stronger constraints on material flow by the surrounding features, especially at low temperatures and/or high forming speeds.

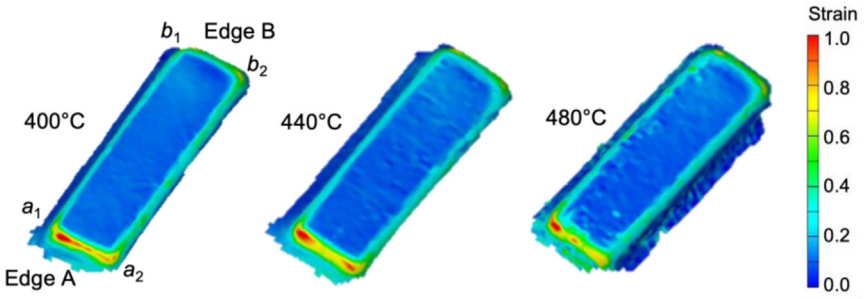

(a) Major strain

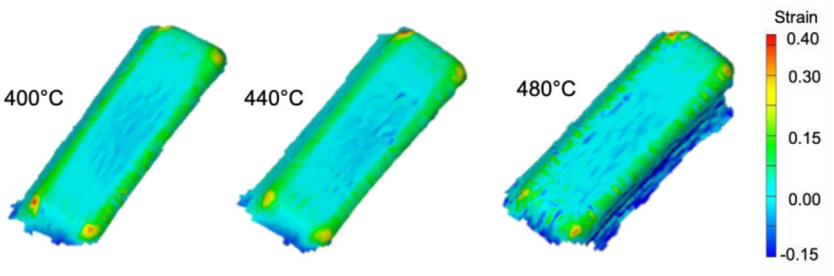

(b) Minor strain

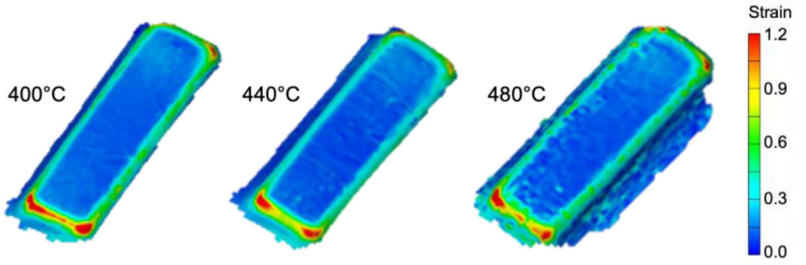

(c) von Mises strain

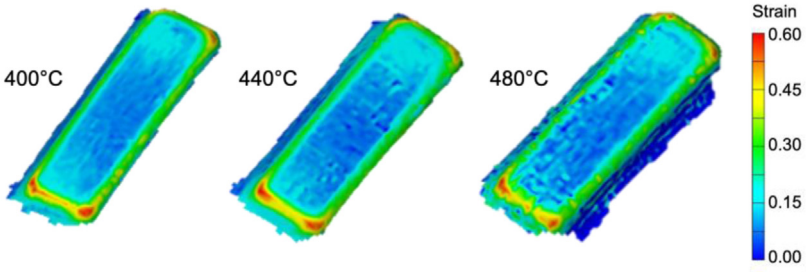

(d) Thickness reduction

Fig. 11. Strain distributions of the components formed at different conditions, constructed using ARGUS technique.

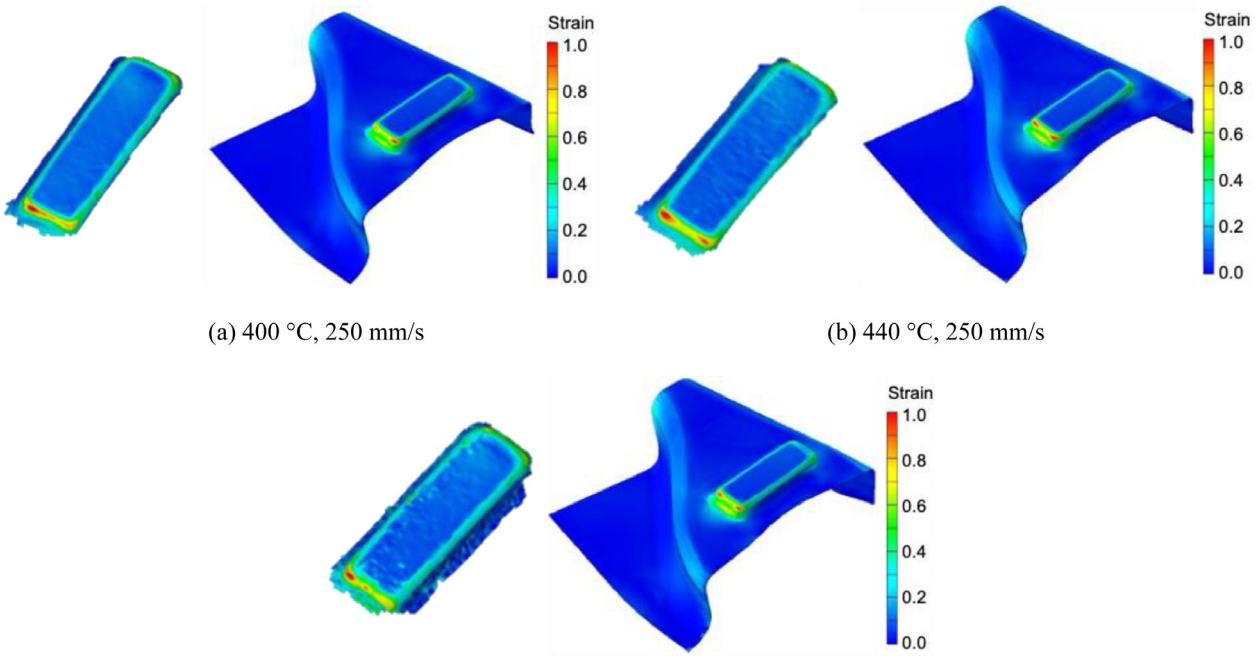

(a) 400 °C, 250 mm/s

(b) 440 °C, 250 mm/s

(c) 480 °C, 250 mm/s

Fig. 12. Experimental (left) and simulated (right) major strain distributions of the components formed under different conditions.

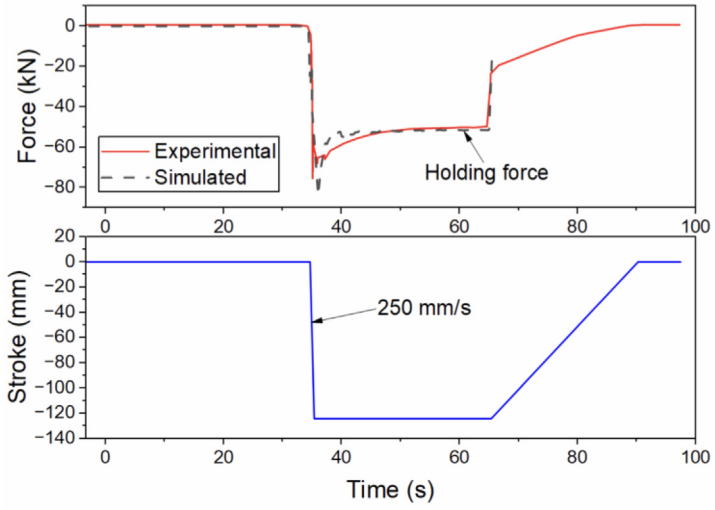

Fig. 13. Force and stroke during B-pillar forming at 440 °C, 250 mm/s.

Table 8. Tested and simulated forming forces.

Forming temperature (°C) / forming speed (mm/s)	Tested holding force (kN)	Simulated holding force (kN)
400 / 250	60.7	66.4
440 / 250	49.4	51.5
480 / 250	37.0	36.2

Acknowledgments

Jiaqi Li appreciates the financial assistance from China Scholarship Council [Grant number: 202008410205].

Funding

This research received no external funding.

Conflicts of interest

The authors have nothing to disclose.

Data availability statement

The data that support the findings of this study are available from the corresponding author upon reasonable request.

Author contribution statement

Conceptualization, J. Lin and Z. Shi; Methodology, J. Li and R. Zhang; Experimental, J. Li; Software, J. Li; Formal Analysis, J. Li; Writing – Original Draft Preparation, J. Li; Writing – Review & Editing, Z. Shi; Supervision, J. Lin and Z. Shi.

References

1. K. Zheng, D.J. Politis, L. Wang, J. Lin, A review on forming techniques for manufacturing lightweight complex-shaped aluminium panel components, Int. J. Lightweight Mater. Manuf. **1** (2018) 55–80
2. J. Lin, T.A. Dean, R.P. Garrett, A process in forming high strength and complex-shaped Al-alloy sheet components, British Patent, WO2008059242 (2008)
3. R.P. Garrett, J. Lin, T.A. Dean, Solution heat treatment and cold die quenching in forming AA 6xxx sheet components: feasibility study, Adv. Mater. Res. –Switz. **6–8** (2005) 673–680
4. R. Gu, Q. Liu, S. Chen, W. Wang, X. Wei, Study on high-temperature mechanical properties and forming limit diagram of 7075 aluminum alloy sheet in hot stamping, J. Mater. Eng. Perform. **28** (2019) 7259–7272
5. K. Nakazima, T. Kikuma, K. Hasuka, Study on the formability of steel sheets, Yawata Tech. Rep. **264** (1968) 8517–8530
6. Z. Marciniak, K. Kuczynski, Limit strains in the processes of stretch-forming sheet metal, Int. J. Mech. Sci. **9** (1967) 609–620
7. Z. Shao, N. Li, J. Lin, T.A. Dean, Development of a new biaxial testing system for generating forming limit diagrams for sheet metals under hot stamping conditions, Exp. Mech. **56** (2016) 1489–1500
8. R. Zhang, Z. Shi, Z. Shao, V.A. Yardley, J. Lin, T.A. Dean, Biaxial test method for determination of FLCs and FFLCs for sheet metals: validation against standard Nakajima method, Int. J. Mech. Sci. **209** (2021) 106694
9. M.A. Ablat, A. Qattawi, Numerical simulation of sheet metal forming: a review, Int. J. Adv. Manuf. Technol. **89** (2017) 1235–1250
10. G. D'Amours, A. Ilinich, Development of a material model for AA7075 aluminium hot stamping, J. Phys.: Conf. Ser. **1063** (2018) 012033
11. Y. Guo, Y. Xie, D. Wang, L. Du, J. Zhao, An improved damage-coupled viscoplastic model for predicting ductile fracture in aluminum alloy at high temperatures, J. Mater. Process. Technol. **296** (2021) 117229
12. R. Zhang, Z. Shi, V.A. Yardley, J. Lin, A CDM-based unified viscoplastic constitutive model of FLCs and FFLCs for boron steel under hot stamping conditions, Int. J. Damage Mech. **31** (2022) 10567895221105655
13. J. Li, R. Zhang, Z. Shi, J. Lin, Characterisation and modelling of thermomechanical behaviour of AA6082 sheet under heterogeneous temperature and strain fields, Int. J. Lightweight Mater. Manuf., https://doi.org/10.1016/j.ijlmm.2025.11.004
14. R. Zhang, Z. Shi, V.A. Yardley, J. Lin, Experimental studies of necking and fracture limits of boron steel sheet under hot stamping conditions, J. Mater. Process. Technol. **302** (2022) 117481
15. X. Kong, X. Chu, C. Chen, Y. Wang, P. Liu, Z. Wang, Comparative investigation of the experimental determination of AA5086 FLCs under different necking criteria, Mater. **14** (2021) 3685
16. M. Merklein, A. Kuppert, M. Geiger, Time dependent determination of forming limit diagrams, CIRP Ann-Manuf. Technol. **59** (2010) 295–298
17. R. Zhang, Z. Shi, Z. Shao, V.A. Yardley, J. Lin, An effective method for determining necking and fracture strains of sheet metals, Methods **8** (2021) 101234
18. R. Zhang, Z. Shi, Z. Shao, T.A. Dean, J. Lin, A novel spatio-temporal method for determining necking and fracture strains of sheet metals, Int. J. Mech. Sci. **189** (2021) 105977
19. X. Song, L. Leotoing, D. Guines, E. Ragneau, Investigation of the forming limit strains at fracture of AA5086 sheets using an in-plane biaxial tensile test, Eng. Fract. Mech. **163** (2016) 130–140
20. J. Lin, T.A. Dean, Modelling of microstructure evolution in hot forming using unified constitutive equations, J. Mater. Process. Technol. **167** (2005) 354–362
21. A.M. Othman, D.R. Hayhurst, B.F. Dyson, Skeletal point stresses in circumferentially notched tension bars undergoing tertiary creep modelled with physically based constitutive equations, Proc. R. Soc. Lond. A **441** (1993) 343–358
22. J. Lin, D.R. Hayhurst, B.F. Dyson, A new design of uniaxial creep testpiece with slit extensometer ridges for improved accuracy of strain measurement, Int. J. Mech. Sci. **35** (1993) 63–78
23. J. Lin, Y. Liu, A set of unified constitutive equations for modelling microstructure evolution in hot deformation, J. Mater. Process. Technol. **143–144** (2003) 281–285

Cite this article as: Jiaqi Li, Zhusheng Shi, Ruiqiang Zhang, Jianguo Lin, Experimental and numerical investigations of sheet AA6082 formability and B-pillar forming under HFQ conditions, Manufacturing Rev. **12**, 28 (2025), https://doi.org/10.1051/mfreview/2025022